

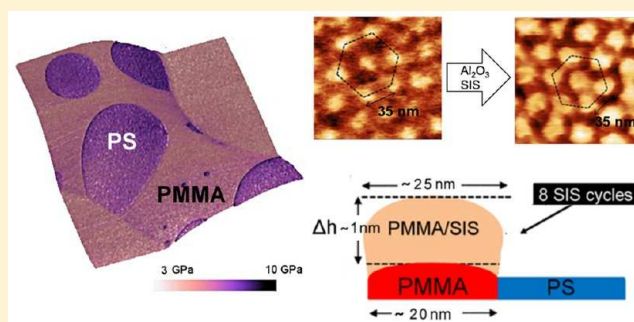
Sequential Infiltration of Self-Assembled Block Copolymers: A Study by Atomic Force Microscopy

Matteo Lorenzoni,^{*,†} Laura Evangelio,[†] Marta Fernández-Regúlez,[†] Célia Nicolet,[‡] Christophe Navarro,[‡] and Francesc Pérez-Murano^{*,†}

[†]Instituto de Microelectrónica de Barcelona (IMB-CNM, CSIC), Campus de la UAB, 08193 Bellaterra, Barcelona, Spain

[‡]Arkema France, R.N. 117, BP34-64170 Lacq, France

ABSTRACT: Sequential infiltration synthesis (SIS), when combined with novel polymeric materials capable of self-assembly, such as block copolymers (BCPs), has been shown to effectively improve the pattern transfer of nanoscale templates. Herein, we present a study of the SIS process aimed at elucidating some critical aspects such as the evolution of the BCP morphology and mechanical properties after infiltration. Atomic force microscopy nanomechanical mapping was able to measure a consistent stiffness change within the SIS-infiltrated poly(methyl methacrylate) (PMMA) blocks. Interestingly, the increase in Young's modulus of the infiltrated blocks is small compared to the final stiffening of the same infiltrated features after a treatment with oxygen plasma.



1. INTRODUCTION

Sequential infiltration synthesis (SIS) consists of an adapted version of atomic layer deposition (ALD) in which the vaporized precursor does not saturate the surface but eventually diffuses and reacts into the bulk material, usually a synthetic or natural polymer. As a result, it yields the selective growth of inorganic materials embedded in a polymeric matrix.¹ SIS recently attracted the attention of researchers because of its potential for nanofabrication when coupled with block copolymers (BCPs) capable of self-assembly.^{2–4} Al₂O₃ SIS using trimethylaluminum (TMA) as a gas precursor is the most studied system, and it has been tested on several polymers,⁵ proving to be an effective method for increasing the tensile strength of natural fibers⁶ and improving the etch resistance of lithography resists such as poly(methyl methacrylate)⁷ (PMMA). During the first step of the SIS process, the precursor (a Lewis acid) diffuses within the film and reacts with PMMA nucleophilic carbonyl and ester groups to form a weakly bonded intermediate complex;⁸ later, water exposure allows Al₂O₃ nucleation. Subsequent cycles can completely saturate PMMA, creating Al₂O₃-modified domains that exhibit enhanced resistance to plasma treatments. The SIS of PMMA has been successfully employed to selectively modify polystyrene-*block*-poly(methyl methacrylate) (PS-*b*-PMMA) BCP thin films.^{1,9,10}

This process has indeed a strong potential for improving pattern transfer, in most cases, BCP thin films do not have enough differential etch selectivity between blocks to be employed as practical lithography materials. Moreover, the self-limiting nature of SIS leads to final features in which changes in volume are minimal¹¹ and can be controlled by varying the number of SIS cycles¹² or other SIS parameters such as

adsorption/purge time or temperature.¹³ With regard to the effect of infiltration on pattern quality, there is evidence of improved line edge roughness⁷ (LER), especially for low- and midfrequency roughness regimes,¹⁴ whereas surface roughness, another sensitive parameter, showed a modest increase after infiltration.¹⁵ Roughness analysis in ref 15 was performed on the top surface of PMMA/SIS sub-100-nm lithographic patterns.

From the perspective of obtaining a reliable method for SIS process characterization, it is important to monitor the changes in morphological and mechanical properties that the infiltrated phase (in this case, PMMA) undergoes after several cycles of SIS, as both types of properties influence the final result after pattern transfer. With regard to lithography-patterned PMMA features (40–110 nm wide), the morphological aspect was clarified by Darling and co-workers¹² in an inspection of SIS-treated PMMA patterns by atomic force microscopy (AFM) and scanning electron microscopy (SEM). Other important elucidations of morphology and defects arise through the use of scanning transmission electron tomography (STEM) for the three-dimensional characterization of self-assembled cylindrical, lamellar, and spherical PS-*b*-PMMA thin films.¹¹

In this work, we evaluated the effects of SIS in PMMA on both micrometer-scale homopolymer droplets and BCP films. From our experience, samples that undergo fewer than five cycles of SIS, under the processing conditions employed here, do not show enough resistance to Si dry etching, resulting in poor pattern transfer. Therefore, we focused on characterizing samples

Received: November 8, 2016

Revised: January 11, 2017

Published: January 17, 2017

exposed to between 5 and 11 cycles of SIS. Other authors,^{9,11} using different SIS process parameters (e.g., lower temperatures or higher chamber pressures during TMA introduction), have limited the number of cycles to 3. It is expected that the higher chamber temperature^{10,13} employed here enhances TMA diffusion out of the film, resulting in the need for further SIS cycles. For details about the SIS process parameters, see the [Materials and Methods](#) section.

AFM is broadly used in surface science to obtain surface topography at the nanometer scale. Additional compositional information can be obtained, for example, from the phase signal when performing AFM in tapping mode. Quantitative nano-mechanical mapping (QNM) can be achieved by performing nanoindentation or collecting conventional force–distance curves,^{16,17} but both approaches present some limitations, namely, excessive indentation depth during nanoindentation and limited acquisition speeds in the collection of force–distance curves. Recently, dynamic modes were successfully used to map the nanomechanical spectra of soft matter surfaces, using higher harmonics,¹⁸ multifrequency excitation,¹⁹ and force reconstruction algorithms.²⁰ Pulsed-force techniques^{21,22} represent an alternative that lies between the above approaches. PeakForce Tapping mode is, in fact, able to acquire a large number of force–distance curves and elaborate them in real time to calculate mechanical properties at each point; the typical, off-resonance working frequency (2 kHz) allows for imaging speeds that are comparable to those of standard tapping mode, and the sample deformation depth is limited to a few nanometers, avoiding resolution loss due to tip damage caused by large tip–sample interactions. With regard to polymers and soft materials in general, this technique has demonstrated great utility: PeakForce Tapping mode can reliably measure the elastic moduli of bulk materials with 50-nm lateral resolution,^{23,24} and it allows for the probing of polymer ultrathin films that are challenging to characterize by any other technique.^{25,26} Some of the samples in this study include PS-*b*-PMMA BCP films forming lamellae and cylindrical structures with characteristic lengths less than 20 nm, and extracting reliable information about such nanoscale domains is possible if proper indentation conditions are employed²⁷ (i.e., to avoid the substrate effect, the so-called “double layer effect”, and plastic deformation). By using PeakForce QNM, we were able to obtain insight into the changes in mechanical properties (Young’s modulus and adhesion) of different SIS samples both at the micrometer scale (homopolymer blends) and at the scale of self-assembled nanodomains (PS-*b*-PMMA BCPs).

2. MATERIALS AND METHODS

2.1. Brush Layer. PS and PS-*r*-PMMA having PS/PMMA volume ratios of 59:41 (R60) and 68:32 (R70), provided by Arkema, were used to form the brush layers. The polymers were dissolved in propylene glycol methyl ether acetate (PGMEA) resulting in a 1.5% (w/w) solution and spin-coated on the substrates. To graft the polymer, samples were annealed for 5 min at 230 °C in a nitrogen atmosphere. Finally, the remaining ungrafted polymer was removed by PGMEA rinsing.

2.2. Homopolymer Blend. The homopolymers employed were PS [$M_n = 38.6 \text{ kg}\cdot\text{mol}^{-1}$, polydispersity index (PDI) = 1.12] and PMMA ($M_n = 38.6 \text{ kg}\cdot\text{mol}^{-1}$, PDI = 1.12). Homopolymer solutions in PGMEA were spin-coated at 2500 rpm for 30 s, forming films of approximately 20 nm. To accelerate the dewetting and phase separation, samples were annealed at 230 °C for 10 min in a nitrogen environment.

2.3. Block Copolymer Self-Assembly. The BCPs employed were provided by Arkema: L37 poly(styrene-*b*-methyl methacrylate) (PS-*b*-PMMA 50:50, $M_n = 79 \text{ kg}\cdot\text{mol}^{-1}$, PDI = 1.13) and C35 poly(styrene-*b*-methyl methacrylate) (PS-*b*-PMMA 69:31, $M_n = 60.8 \text{ kg}\cdot\text{mol}^{-1}$, PDI = 1.09), where L indicates lamellae and C indicates cylinders resulting in the final self-assembly and the number represents the nominal pitch, L_0 . Each PS-*b*-PMMA powder was dissolved in PGMEA, resulting in 1.5% (w/w) solutions. The block copolymer solutions were spin-coated onto the brush layer to obtain films with the desired uniform thickness. Samples were then annealed for 10 min at 230 °C in nitrogen to induce self-assembly.

2.4. Sequential Infiltration Synthesis. Alumina was synthesized using binary reactions of trimethylaluminum (TMA, Aldrich, 97%) and water at 135 °C. The complete SIS process was performed as follows: First, chamber stabilization with nitrogen was performed for 10 min. Then, the precursor, TMA, was admitted into the reactor at 0.5 Torr for 60 s. Afterward, the chamber was purged with nitrogen for 80 s. The same procedure was repeated for water. This entire sequence was repeated cyclically.

2.5. AFM. To obtain surface topography and elastic modulus maps, we used a Dimension Icon microscope (Bruker Inc.) operated in normal soft tapping mode (200-nm free oscillation amplitude with a set point above 70%) or in PeakForce tapping mode. The cantilevers employed were standard tapping cantilevers (TESPAR3; nominal tip radius of 7 nm) with a nominal spring constant value of $k = 26 \text{ N/m}$. The sample Young’s modulus ($1 \text{ GPa} < E < 10 \text{ GPa}$) determines the cantilever spring constant to choose to obtain detectable deformation. The applied force set points ranged between 10 and 25 nN; in particular, the force set point was adjusted to obtain optimal deformation for a reliable fit (1–2 nm) and not to produce plastic deformation.²⁶ Further details about the experimental procedure for the imaging of BCP thin films are well described in refs 26 and 27. During measurements in PeakForce Tapping mode, the tip oscillates at 2 kHz. Information about the indentation force and material response was collected for each individual oscillation. By a careful calibration of the cantilever spring constant and tip radius (see ref 27 for details), force–distance curves are able to provide reliable quantitative information at the nanoscale,²⁸ such as elastic modulus, adhesion force, and sample deformation.

The curves were fitted with the Derjaguin–Muller–Toporov (DMT) model,¹⁶ derived from a Hertzian model that takes adhesive forces into account. It is applicable for systems with low adhesion and small tip radii, using a portion of the unload curve as the fit region. The relationship between the applied load and the reduced modulus E^* is given by

$$F = \frac{4}{3}E\sqrt{Rd^3} + F_{\text{adh}} \quad (1)$$

where F is the force, R is the tip radius, d is the deformation, F_{adh} is the maximum adhesion force, and z is the vertical displacement. The relationship between the reduced modulus E^* and the sample modulus E_s can be expressed as

$$\frac{1}{E^*} = \frac{1 - \nu_t^2}{E_t} + \frac{1 - \nu_s^2}{E_s} \quad (2)$$

In our case, a Si tip has a Young’s modulus, E_t , ranging from 160 to 190 GPa, and the sample Poisson’s ratio, ν_s , can be approximated as 0.3, giving $E_s \approx 0.88E^*$. For clarity, in this

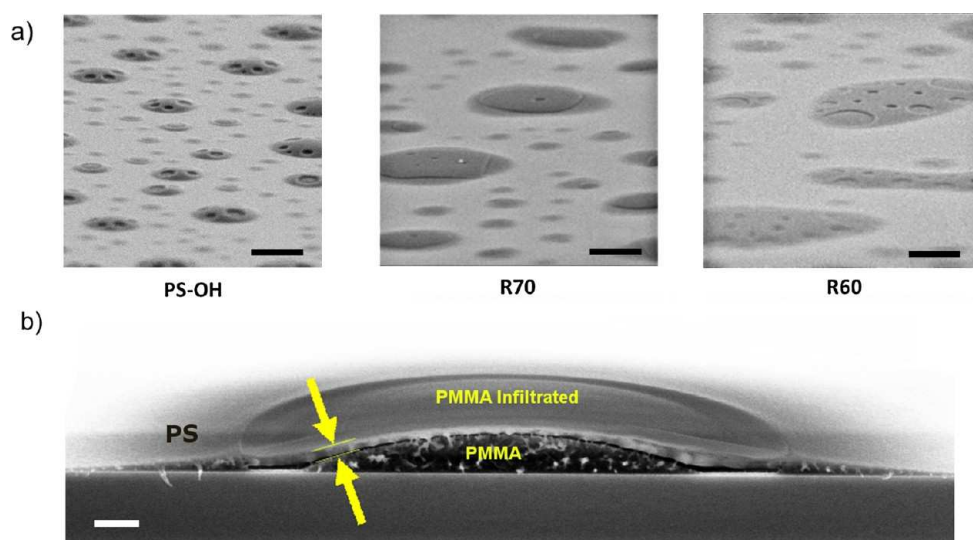


Figure 1. (a) SEM images of polymer blend droplets (PS/PMMA) on three different brushes, showing different dewetting behaviors as the percentage of PMMA in the brush layer increases. Images on top of PS–OH and R70 were recorded after an oxygen plasma treatment intended to remove PMMA. Scale bar = 2 μm . (b) SEM image of a cross section of a PS/PMMA droplet after five SIS cycles. A central darker PMMA circular island is surrounded by PS. The contrast in the cross section reveals the extent of SIS within PMMA (80–90 nm), as indicated by the yellow arrows. Scale bar = 200 nm.

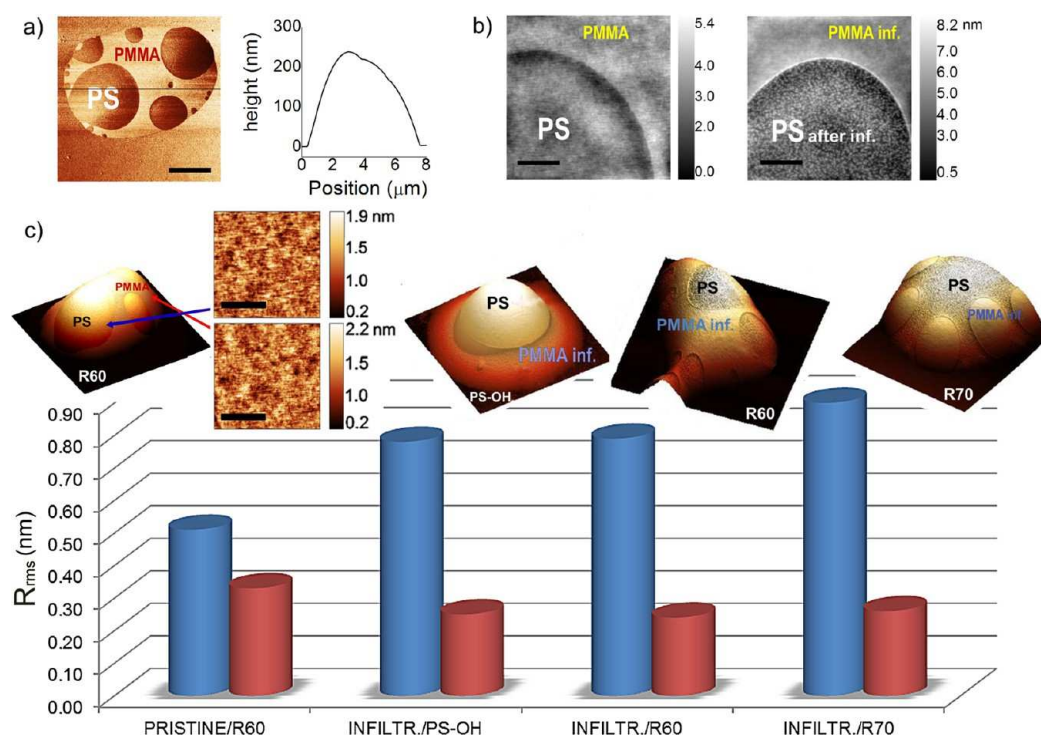


Figure 2. Morphological comparison of PS/PMMA blend droplets deposited on different brushes. (a) AFM phase image of a blend droplet on an R60 brush, where darker areas are smaller PS droplets, and PMMA is lighter in color. On the right side, the height profile of the droplet is also reported. Scale bar = 2 μm . (b) Height maps of the central area of a droplet (left) before and (right) after five SIS cycles. After infiltration, the PS present a rougher surface as a result of the creation of alumina particles. Scale bar = 500 nm. (c) AFM three-dimensional height map representation of blend droplets on different brushes. AFM detailed topographies of 1.4 μm^2 areas taken from the droplet surface were used to calculate surface roughness (R_{rms}). For each sample, PMMA (blue) and PS (red) R_{rms} values are presented in the chart. Scale bar = 500 nm.

work, the figures and color maps always report E_s values. Topography images were subjected to a polynomial flattening to correct the surface tilt and enhance the contrast of interesting features. Surface topographies acquired in tapping mode were reconstructed with the freeware program Gwyddion²⁹ to partially correct the influence of the tip on the image data.

3. RESULTS AND DISCUSSION

3.1. Infiltrated PS and PMMA Homopolymer Films. As a first step, we studied the effects of five SIS cycles on a homopolymer PS/PMMA blend deposited on different brushes in such a way that droplets formed easily after dewetting. After an annealing of 10 min at 230 $^{\circ}\text{C}$, the final morphology of the surface consisted of semispherical micrometer-scale droplets, in

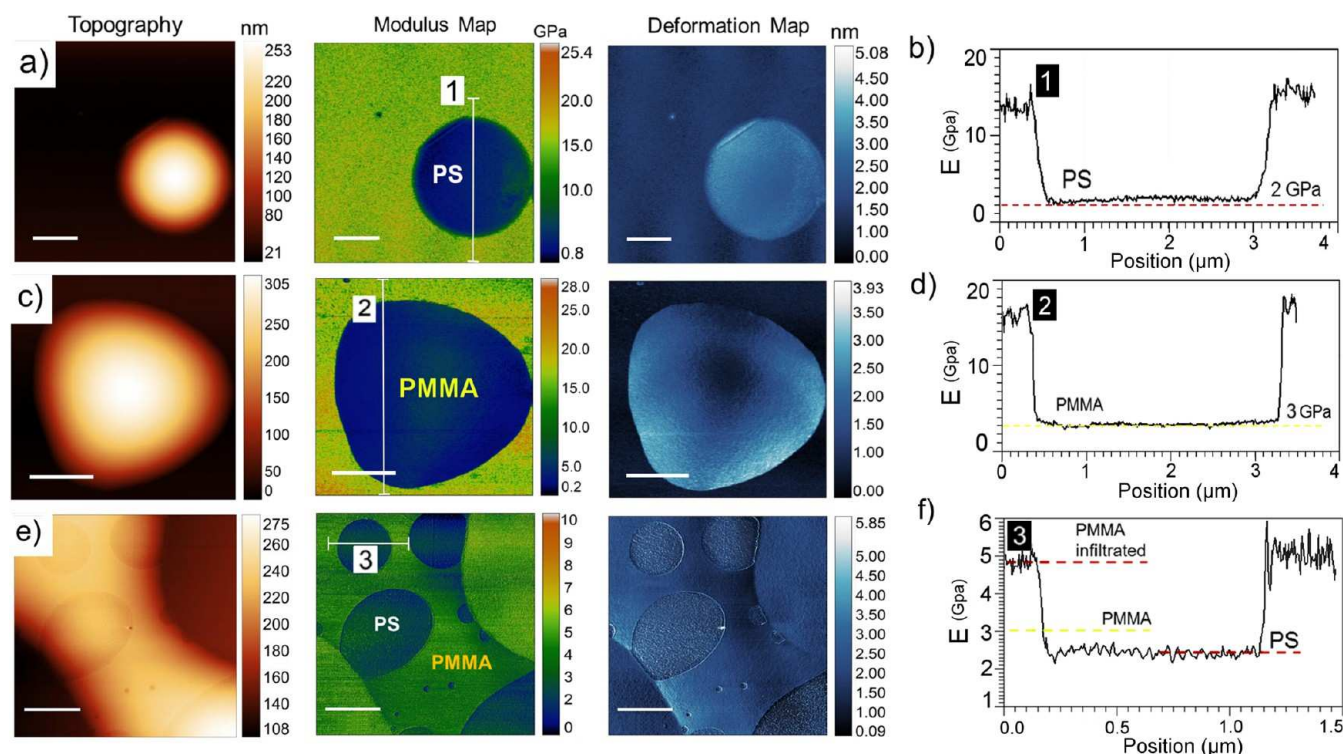


Figure 3. (a,c,e) AFM topography, Young's modulus, and deformation maps of (a) a PS droplet, (c) a PMMA droplet, and (e) the homopolymer blend after SIS. (b,d,f) Profiles reporting the value of the Young's modulus for (b) PS, (d) PMMA, and (f) infiltrated PMMA. Deformation maps show that the samples were probed under similar conditions. The set-point force was set at 20 nN for all samples. From panel f, one can appreciate the increase in stiffness of the PMMA phase due to five cycles of SIS. The PMMA droplet surface E changes from 3.0 ± 0.5 to 5.3 ± 0.7 GPa. The PS surface modulus tends to be less affected (even showing an apparent softening), changing from 2.6 ± 0.3 to 2.2 ± 0.4 GPa. The value reported is the average E value along the 10 line profiles. Scale bar = $1 \mu\text{m}$.

which the two blend components were easily distinguishable. Figure 1a shows how the dewetting behavior changed when the fraction of PMMA in the brush was increased. The relative affinity of the surface for the two blocks defines the contact angle of the droplets with the substrate and, thus, the final morphology of the film after annealing. On top of brush films with greater affinity for PS (PS-OH and R70), PS formed large drops, which, in turn, incorporated smaller PMMA droplets. When the blend was deposited on top of R60, the opposite behavior occurred, with large PMMA droplets tending to incorporate smaller PS droplets. Figure 1b shows an SEM cross-sectional image of a droplet formed on a PS-OH brush and subjected to five SIS cycles. In this case, a central island of infiltrated PMMA was surrounded by a larger PS region. The image allows for a rough estimation of the infiltration depth (80–90 nm), as it presents a clear distinction between the darker pristine PMMA and the lighter gray infiltrated PMMA. The infiltration thickness was less than the 200–300 nm reported previously for similar infiltration conditions⁷ but still ensured that the SIS process completely saturated the BCP thin films, whose thicknesses were usually less than 50 nm.

Homopolymer blends, before and after SIS, were analyzed by AFM. The results are presented in Figure 2. A clear phase contrast allows for the identification of the two components of a noninfiltrated sample (Figure 2a). A height profile is also given in Figure 2a to appreciate the size of the droplet. Panel b of Figure 2 shows that the PMMA root-mean-square roughness (R_{rms}) remained substantially unaffected by the five SIS cycles. The R_{rms} value was calculated after the flattening of the topography (thus the subtraction of the droplet curvature): It remained less than

0.25 nm in all three samples deposited on the different brush layers. Sample morphology and roughness values are summarized in panel c of Figure 2. The main feature is that the PS surface showed a consistent increase in surface roughness after SIS, due to the nucleation of Al_2O_3 clusters. In contrast, the surface roughness of the infiltrated PMMA areas exhibited a small decrease.

In the determination of nanomechanical properties, micrometer-size homopolymer droplets present the advantage that high lateral resolution is not needed, and as a result, a duller AFM tip can be used to increase contact area. In this way, the data are more accurate and can be compared to the results obtained from nanoindentation or macroscopic measurements.²⁴ In Figure 3, we summarize the results from the investigation of three samples: a PS droplet (Figure 3a,b), a PMMA droplet (Figure 3c,d), and a blend of the two components after infiltration (Figure 3e,f). We found that the surface modulus of the PMMA droplets increased from 3.0 ± 0.5 to 5.3 ± 0.7 GPa after five cycles of SIS. This relatively low increase is compatible with the diffusion of the TMA precursor (for five SIS cycles, PMMA carbonyl sites should be saturated¹) and the incorporation of Al_2O_3 within the polymer without the creation of a continuous scaffolding. On the contrary, the PS surface stiffness was less affected (even showing an apparent softening), changing from 2.6 ± 0.3 to 2.2 ± 0.4 GPa.

3.2. Infiltrated PS-*b*-PMMA Self-Assembled Films. Two types of PS-*b*-PMMA films were investigated: C35 (vertical cylinders) and L37 (vertical lamellae). Starting with cylinders, Figure 4 shows the changes in surface morphology as a function of the number of SIS cycles. From the SEM images in Figure 4, one can clearly observe a reversal in contrast: Vertical PMMA

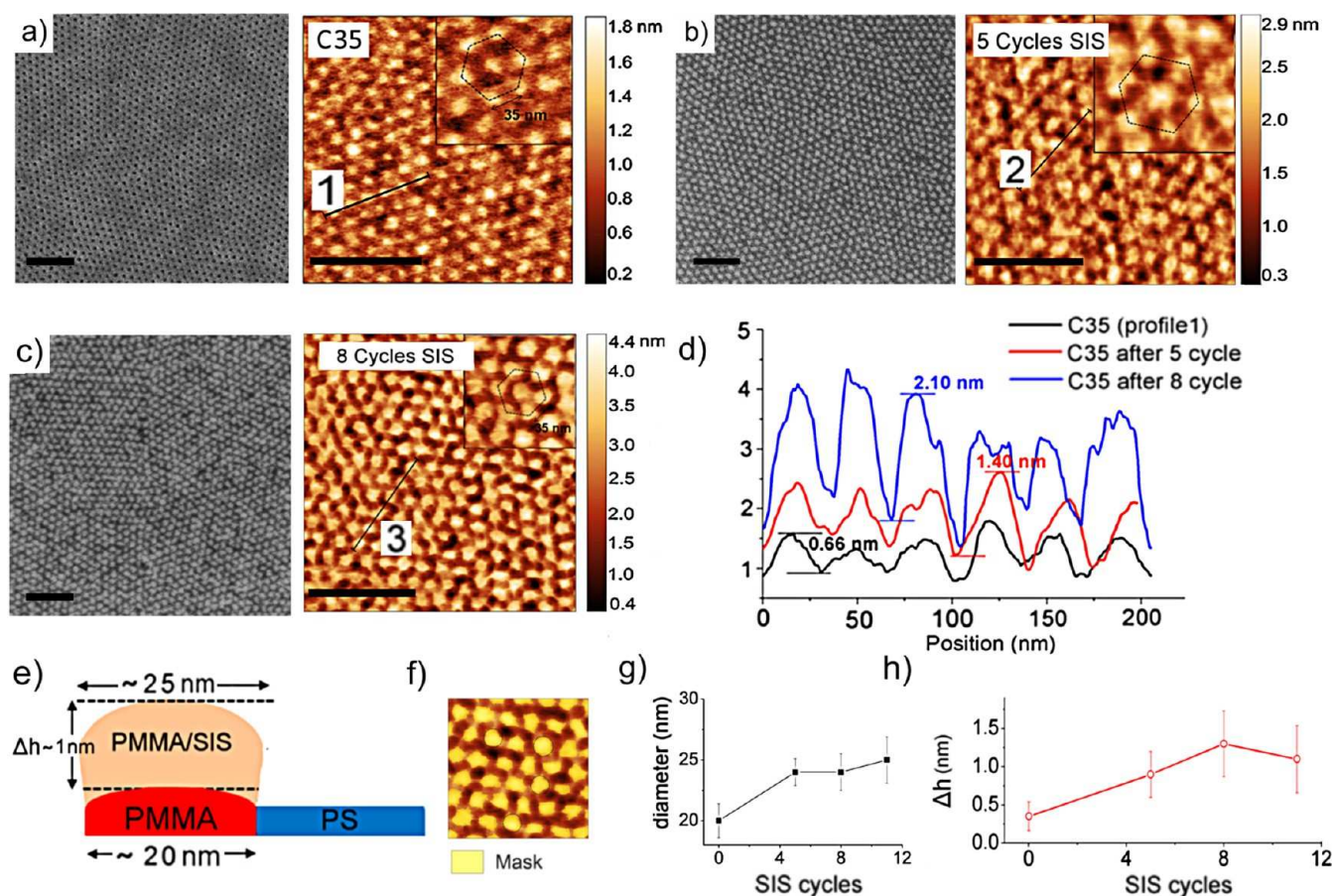


Figure 4. Comparison of SEM images of C35 BCP samples: (a) pristine and (b,c) infiltrated by (b) five and (c) eight SIS cycles. SEM top views show how, in the pristine film (without PMMA), cylinders appear as dark spots. We also notice a switch in contrast (vertical infiltrated PMMA cylinders appear as brighter spots after SIS) and a widening of the infiltrated area. Next to each SEM top view are shown AFM topography maps. Images were acquired in tapping mode. Vertical PMMA cylinders are disposed in a hexagonal lattice, as shown in each inset. All scale bars represent 200 nm. (d) Comparison of height profiles, showing progressive swelling due to SIS. (e) Schematic representation of the overall effect of eight SIS cycles: A single PMMA cylinder is likely to increase its height by approximately 1 nm and to widen its diameter by 25% within the first five cycles. (f) Topography masked by the Otsu method, identifying the PMMA domains (details in the main text). (g,h) Changes in (g) cylinder diameter and (h) cylinder height as a function of the number of cycles.

cylinders appear as darker spots in Figure 4a (pristine C35) and as brighter spots in Figure 4b (after five cycles of SIS) and Figure 4c (after eight cycles of SIS). Top-view SEM images already provide a clear indication that the PMMA domains tended to become wider after each cycle. This phenomenon was quantified through the analysis of AFM images, as described later.

With a methodology similar to that presented in the previous section, we studied the morphologies of the BCP self-assembled films after infiltration. First, we employed AFM in tapping mode under conditions such that the tip–surface interaction was minimized (“soft” tapping mode, where the tip–surface interaction is dominated by attractive forces), and then we probed the same samples in PeakForce Tapping mode to obtain maps of mechanical properties at the nanoscale. Through comparisons of the results of the two types of experiments, it can be ensured that (i) the topographical information acquired in soft tapping mode is not affected by local deformation and (ii) the deformation exerted during the PeakForce scan is not plastically modifying the sample.

From the topographic images, we determined that the infiltrated PMMA tended to swell.¹² The pristine C35 film presented PMMA domains that were slightly elevated with respect to the PS matrix, with a difference in height (Δh) of

approximately 0.35 nm. (This average Δh value was obtained by threshold masking of the AFM height image according to the Otsu method.³⁰) The height difference was approximately 1 nm within the first five cycles. For a larger number of cycles up to 11 SIS cycles, the increase in height was less pronounced (Figure 4d,h). The slow increase in apparent height after five SIS cycles was probably due to the accumulation of alumina on top of the PMMA/SIS phase. These results confirm that the swelling of the PMMA domains was self-limited¹ and that it reached saturation within a few (five) SIS cycles.

The diameter of the PMMA cylinders showed a similar behavior (Figure 4g). The value of the diameter was obtained by performing a grain analysis (equivalent grain radius of more than 150 masked areas) after surface reconstruction and masking the whole AFM height image according to the Otsu method (Figure 4f). The measured diameter for the pristine sample was 20.5 ± 1.4 nm, which is in good agreement with the expected value of 19.5 nm.³¹ After five cycles, the PMMA/SIS cylinder diameter increased by approximately 4 nm, and no significant additional increase was observed after adding more cycles. The overall effect on the PMMA cylinders after eight SIS cycles is schematized in Figure 4e. The main morphological change that occurred after more than five SIS cycles was the formation of tiny bridges

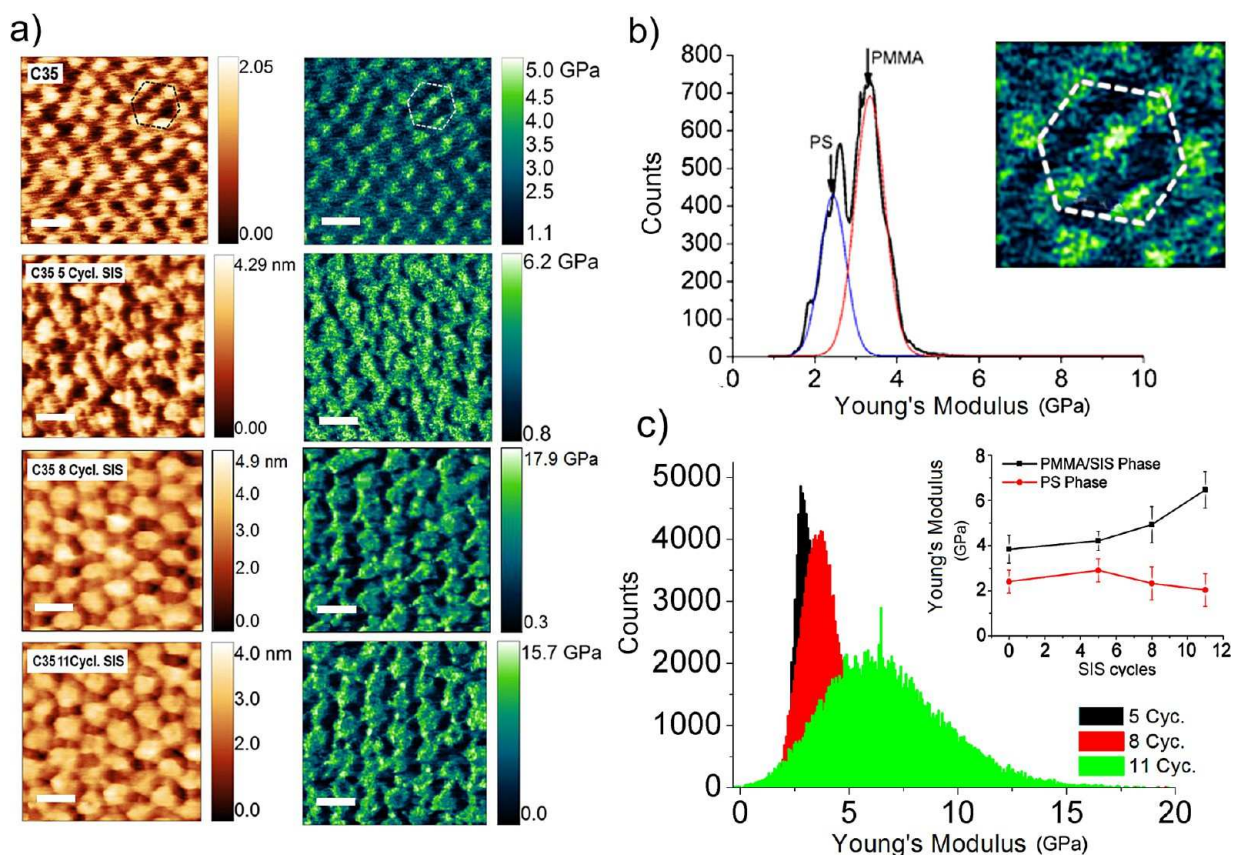


Figure 5. (a) Topography and corresponding Young's modulus maps of C35 BCP samples, from the pristine surface to surfaces subjected to 5, 8, and 11 SIS cycles. Surface morphology changes according to the schematic shown in Figure 4e. Stiffer PMMA domains (light green) are visible in all images. All scale bars represent 50 nm. (b) Modulus distribution of a pristine sample, with a clear distinction between PS and PMMA domains. Inset: Resolved E map of a hexagonal cell of vertical cylinders (light green). (c) Tendency of the modulus of the PMMA cylinders to increase with SIS. Inset: Summary of the values of the Young's moduli of the two phases as a function of the number of SIS cycles. The color scale of modulus maps (infiltrated samples) is nonlinear.

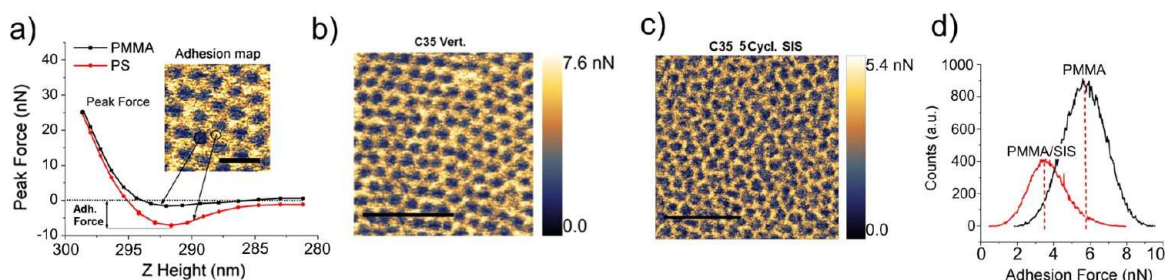


Figure 6. (a) Force–distance curves acquired on PS and PMMA nanodomains; the red dotted curve (PS) presents higher adhesion. (b,c) Adhesion force maps comparing (b) a pristine sample with (c) a sample subjected to five cycles of SIS, confirming that the PS surface is not involved in SIS whereas the PMMA phase shows a shift in adhesion. (d) Two distributions of adhesion force values for PMMA obtained from each scan: pristine (black curve) and infiltrated (red curve). The color scales of panels b and c are nonlinear. Scale bar = 200 nm.

between the PMMA/SIS phases, probably due to the nucleation of alumina clusters on the PS, as was observed on top of the homopolymer microdroplets.

The fact that exceeding a certain number of SIS cycles (five in our case) led to the formation of a thin top layer of alumina was also confirmed by images recorded in PeakForce Tapping mode. Figure 5a shows 250×250 nm height and modulus maps of C35 samples ranging from the pristine film to films subjected to 5, 8, and 11 SIS cycles. The value of the Young's modulus that we report is the average of the region masked by the height threshold mask (as reported in Figure 4f). Figure 5b shows the modulus distribution of the pristine film in which PS and PMMA domains

are clearly resolved. The evolution of the Young's modulus of the infiltrated PMMA phase after increasing numbers of SIS cycles is presented in Figure 5c. Whereas the stiffness of the PS phase remained constant upon infiltration (~ 2.4 GPa), the modulus of the PMMA/SIS phase increased consistently over 11 SIS cycles (Figure 5c) from approximately 3.8 GPa (pristine) to 6.5 ± 0.7 GPa. All maps were acquired with the same tip at a constant force set point of 10 nN, inducing an average deformation ranging from 0.8 to 1.3 nm. This increase is compatible with the creation of a thin cap of stiff material localized on PMMA/SIS domains²⁶ in samples subjected to more than five SIS cycles. Examples of the force curves acquired on the PS and PMMA domains are

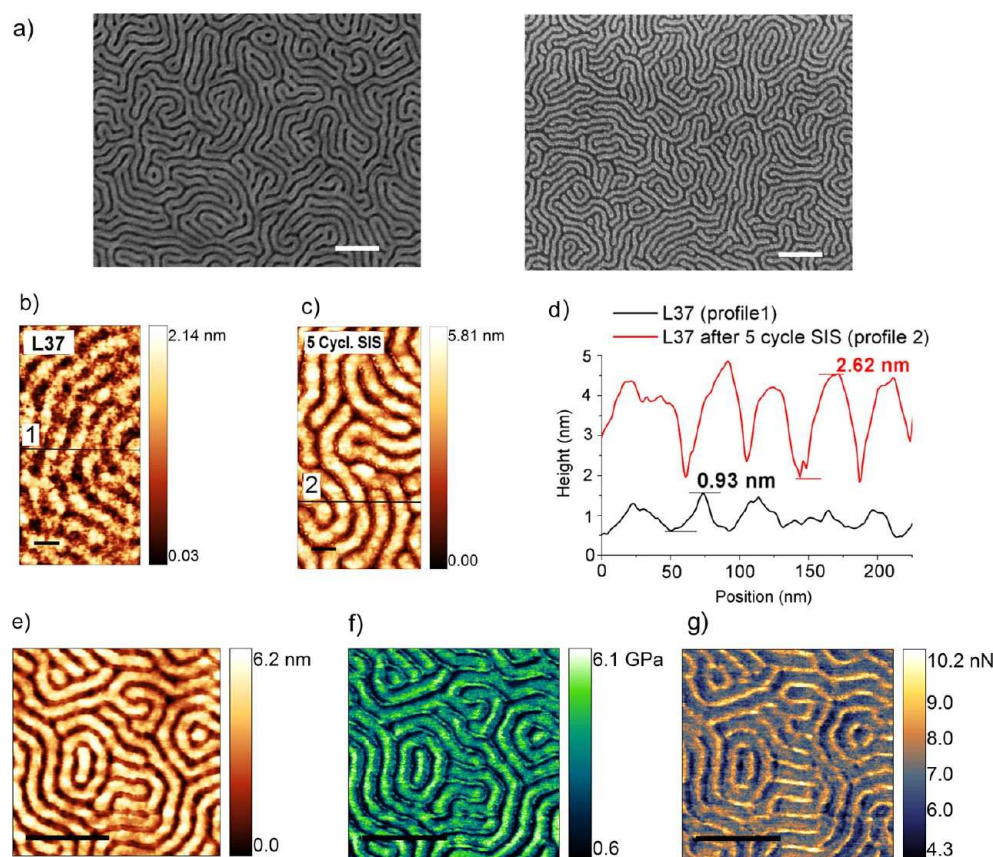


Figure 7. (a) SEM top views of vertical lamellae in fingerprint orientation obtained with L37 PS-*b*-PMMA BCP. SIS-infiltrated lamellae tend to show a higher contrast: What appears dark in the left panel (PMMA plasma-removed domains) is instead brighter when imaging an infiltrated sample. Scale bar = 200 nm. (b,c) AFM topography acquired in tapping mode of L37 PS-*b*-PMMA BCP samples with random lamellae in vertical configuration: (b) pristine and (c) treated with five SIS cycles. (d) Two height profiles confirming PMMA swelling due to SIS. Scale bar = 50 nm. (e–g) Topography, modulus map, and adhesion map, respectively, acquired in PeakForce Tapping mode. As expected, the infiltrated PMMA phase (light green in the modulus map) shows the reverse contrast in the adhesion map. The color scales in panels e and f are nonlinear. All scale bars represent 200 nm.

presented in Figure 6a. The most visible difference in this set of curves (taken at a higher set-point force to enhance contrast) occurs in the region below zero force where attractive forces are dominant; the most negative value of the force was used to calculate the adhesion force.

Adhesion force maps comparing the pristine sample and the sample subjected to five SIS cycles (Figure 6b–d) confirmed that the PS surface remained unmodified during SIS whereas the PMMA phase exhibited lower adhesion (Figure 6d) after being infiltrated. This small shift is depicted in Figure 6d, where the two distributions of adhesion force values for PMMA obtained from each scan, pristine (black curve) and infiltrated (red curve), are reported.

We performed similar characterization of the L37 PS-*b*-PMMA BCP with lamellae in both random and aligned configurations (Figures 7 and 8, respectively). We analyzed the effects of infiltration on samples subjected to five SIS cycles. The SEM images before and after SIS show a switch in contrast (Figure 7a), as occurred for the PS-*b*-PMMA BCP forming vertical cylinders (C35 samples). AFM topography shows a swelling in the range of what was found for C35 (Figure 7b–d) with the peak–valley distance changing from 0.8–0.9 nm to approximately 2.5 nm. Figure 7e–g presents a high-resolution PeakForce Tapping scan of L37 in the fingerprint orientation. A modest increase in stiffness (PMMA/SIS phase stiffness = 3.6 ± 0.4 GPa) was also measured, which is consistent with the findings on cylindrical BCPs examined previously.

PeakForce Tapping mode imaging was performed on an L37 aligned (directed self-assembly) sample subjected to five SIS cycles (Figure 8). This sample was subjected to a further step, consisting of an oxygen plasma etching process to remove the PS block. In Figure 8a–c, we show topographic and modulus maps of the vertically aligned infiltrated PMMA stripes. Interestingly, the oxygen plasma treatment induced a significant increase in stiffness (Figure 8d) with a distribution of the Young's modulus values centered at about 13.6 GPa (red area), much greater than the modulus distribution before the plasma treatment (green area), which was centered at about 3.6 GPa. The map was acquired at 10 nN. To obtain the Young's modulus distribution, we first masked the topography by height threshold set at 50% (inset of Figure 8b), and then we transferred the mask to the modulus image. The increase in stiffness during the TMA/water cycles is likely to have been due to the creation of a hybrid material¹³ in which Al₂O₃ was dispersed in the polymeric matrix. The subsequent plasma treatment not only removed the polymeric portion of the film but also seems to have promoted the densification of the Al₂O₃ clusters into a stable network,⁹ as suggested by the significant stiffening revealed in the final measurements. To confirm this hypothesis, we removed the PMMA blocks of a pristine sample by oxygen plasma treatment and measured the stiffness of the remaining PS blocks. The plasma seemed not to have affected the resulting stiffness, as the modulus of the L37 PS phase after oxygen stripping revealed a

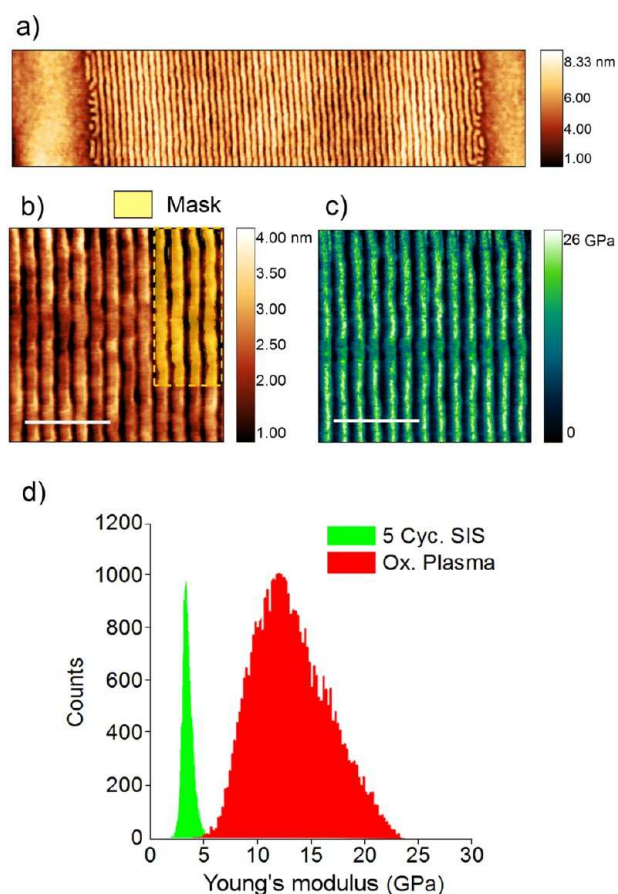


Figure 8. AFM topography images of L37 aligned samples subjected to five SIS cycles. (a) Topography of a wide stripe of aligned lamellae. (b) Topography of a smaller area (500×500 nm) showing the height mask used to extract E values, which are mapped in panel c. (d) Young's modulus histograms comparing the E values PMMA blocks before (green) and after (red) oxygen plasma treatment. Scale bar = 200 nm.

slight increase in Young's modulus that was not comparable to the increase in stiffness of the SIS-infiltrated samples.

4. CONCLUSIONS

In conclusion, we have shown the impact of sequential infiltration synthesis on the morphology and mechanical properties of PS-*b*-PMMA BCPs by AFM characterization. We have demonstrated that the methodology is adequate for determining the optimal SIS process conditions. The results confirmed that the optimal number of SIS cycles under the processing conditions used in the present work was between 5 and 11 but that, after more than five SIS cycles, the appearance of alumina bridges between PMMA features was induced. The PMMA surface roughness remained substantially unaffected by a few SIS cycles, whereas the PS surface could eventually show roughening as a result of the nucleation of Al_2O_3 grains. We confirmed that the swelling due to SIS was self-limited and

reached saturation in a few (five) cycles; for more than five cycles, the formation of alumina networks tended to progress on the surface connecting the PMMA domains.

The results of the determination of the Young's modulus are summarized in Table 1. Infiltration was found to increase the PMMA stiffness (40–70%) but to leave the PS elastic modulus substantially unaffected. No major differences were found in the resulting properties of the blocks depending on whether the infiltrated films consisted of vertical cylinders or lamellae. The increase in Young's modulus of the infiltrated phase was modest compared to the final stiffening after treatment with oxygen plasma, suggesting that further densification of the alumina domains occurred during exposure to oxygen plasma.

AUTHOR INFORMATION

Corresponding Authors

*Tel.: +34 93 594 77 00 (ext. 2114). E-mail: matteo.lorenzoni@imb-cnm.csic.es.

*Tel.: +34 93 594 77 00 (ext. 2114). E-mail: Francesc.Perez@csic.es.

ORCID

Matteo Lorenzoni: 0000-0002-4933-5704

Notes

The authors declare no competing financial interest.

ACKNOWLEDGMENTS

This work was partially funded by the projects CoLISA.MMP (ICT Project 619793), PLACYD (ENIAC 621217 and PCIN-2013-033 MINECO), and FORCE-for-FUTURE (CSD2010-00024). L.E. acknowledges the Ministry of Education of Spain for her FPU grant (FPU 13/03746).

REFERENCES

- (1) Peng, Q.; Tseng, Y. C.; Darling, S. B.; Elam, J. W. Nanoscopic Patterned Materials with Tunable Dimensions via Atomic Layer Deposition on Block Copolymers. *Adv. Mater.* **2010**, *22*, 5129–5133.
- (2) Stoykovich, M. P.; Nealey, P. F. Block Copolymers and Conventional Lithography. *Mater. Today* **2006**, *9*, 20–29.
- (3) Choi, J. W.; Li, Z.; Black, C. T.; Sweat, D. P.; Wang, X.; Gopalan, P. Patterning at the 10 Nanometer Length Scale Using a Strongly Segregating Block Copolymer Thin Film and Vapor Phase Infiltration of Inorganic Precursors. *Nanoscale* **2016**, *8*, 11595–11601.
- (4) Ishchenko, O. M.; Krishnamoorthy, S.; Valle, N.; Guillot, J.; Turek, P.; Fechete, I.; Lenoble, D. Investigating Sequential Vapor Infiltration Synthesis on Block-Copolymer-Templated Titania Nanoarrays. *J. Phys. Chem. C* **2016**, *120*, 7067–7076.
- (5) Gong, B.; Parsons, G. N. Quantitative in Situ Infrared Analysis of Reactions between Trimethylaluminum and Polymers during Al_2O_3 Atomic Layer Deposition. *J. Mater. Chem.* **2012**, *22*, 15672.
- (6) Lee, S. M.; Pippel, E.; Moutanabbir, O.; Kim, J. H.; Lee, H. J.; Knez, M. In Situ Raman Spectroscopic Study of Al-Infiltrated Spider Dragline Silk under Tensile Deformation. *ACS Appl. Mater. Interfaces* **2014**, *6*, 16827–16834.
- (7) Tseng, Y.-C.; Peng, Q.; Ocola, L. E.; Czaplowski, D. A.; Elam, J. W.; Darling, S. B. Enhanced Polymeric Lithography Resists via Sequential Infiltration Synthesis. *J. Mater. Chem.* **2011**, *21*, 11722–11725.

Table 1. Summary of Measured E Values after Different Processes

sample		homopolymer blends	cylinders	lamellae	lamellae + oxygen plasma
pristine	PS	2.6 ± 0.3	2.4 ± 0.2	2.0 ± 0.2	4.2 ± 0.4
	PMMA	3.0 ± 0.5	3.8 ± 0.6	2.8 ± 0.7	–
five SIS cycles	PS	2.2 ± 0.4	2.9 ± 0.5	3.1 ± 0.4	–
	PMMA	5.3 ± 0.7	4.2 ± 0.4	3.6 ± 0.4	13.6 ± 1.6

- (8) Biswas, M.; Libera, J. A.; Darling, S. B.; Elam, J. W. New Insight into the Mechanism of Sequential Infiltration Synthesis from Infrared Spectroscopy. *Chem. Mater.* **2014**, *26*, 6135–6141.
- (9) Ruiz, R.; Wan, L.; Lille, J.; Patel, K. C.; Dobisz, E.; Johnston, D. E.; Kisslinger, K.; Black, C. T. Image Quality and Pattern Transfer in Directed Self Assembly with Block-Selective Atomic Layer Deposition. *J. Vac. Sci. Technol., B: Nanotechnol. Microelectron.: Mater., Process., Meas., Phenom.* **2012**, *30*, 06F202.
- (10) Tseng, Y. C.; Peng, Q.; Ocola, L. E.; Elam, J. W.; Darling, S. B. Enhanced Block Copolymer Lithography Using Sequential Infiltration Synthesis. *J. Phys. Chem. C* **2011**, *115*, 17725–17729.
- (11) Segal-Peretz, T.; Winterstein, J.; Doxastakis, M.; Ramírez-Hernández, A.; Biswas, M.; Ren, J.; Suh, H. S.; Darling, S. B.; Liddle, J. A.; Elam, J. W.; et al. Characterizing the Three-Dimensional Structure of Block Copolymers via Sequential Infiltration Synthesis and Scanning Transmission Electron Tomography. *ACS Nano* **2015**, *9*, 5333–5347.
- (12) Tseng, Y. C.; Mane, A. U.; Elam, J. W.; Darling, S. B. Enhanced Lithographic Imaging Layer Meets Semiconductor Manufacturing Specification a Decade Early. *Adv. Mater.* **2012**, *24*, 2608–2613.
- (13) Biswas, M.; Libera, J. A.; Darling, S. B.; Elam, J. W. Kinetics for the Sequential Infiltration Synthesis of Alumina in Poly(methyl Methacrylate): An Infrared Spectroscopic Study. *J. Phys. Chem. C* **2015**, *119*, 14585–14592.
- (14) Singh, A.; Knaepen, W.; Sayan, S.; el Oteff, Z.; Chan, B. T.; Maes, J. W.; Gronheid, R. Impact of Sequential Infiltration Synthesis on Pattern Fidelity of DSA Lines. *Proc. SPIE* **2015**, *9425*, 94250N–7.
- (15) Tseng, Y.-C.; Peng, Q.; Ocola, L. E.; Czaplowski, D. a.; Elam, J. W.; Darling, S. B. Etch Properties of Resists Modified by Sequential Infiltration Synthesis. *J. Vac. Sci. Technol., B: Nanotechnol. Microelectron.: Mater., Process., Meas., Phenom.* **2011**, *29*, 06FG01.
- (16) Cappella, B.; Dietler, G. Force–Distance Curves by Atomic Force Microscopy. *Surf. Sci. Rep.* **1999**, *34*, 1–104.
- (17) Wang, D.; Fujinami, S.; Liu, H.; Nakajima, K.; Nishi, T. Investigation of True Surface Morphology and Nanomechanical Properties of Poly(styrene-*B*-Ethylene-Co-Butylene-*B*-Styrene) Using Nanomechanical Mapping: Effects of Composition. *Macromolecules* **2010**, *43*, 9049–9055.
- (18) Raman, A.; Trigueros, S.; Cartagena, A.; Stevenson, a. P. Z.; Susilo, M.; Nauman, E.; Contera, S. A. Mapping Nanomechanical Properties of Live Cells Using Multi-Harmonic Atomic Force Microscopy. *Nat. Nanotechnol.* **2011**, *6*, 809–814.
- (19) Herruzo, E. T.; Perrino, A. P.; Garcia, R. Fast Nanomechanical Spectroscopy of Soft Matter. *Nat. Commun.* **2014**, *5*, 3126.
- (20) Payam, A. F.; Martin-Jimenez, D.; Garcia, R. Force Reconstruction from Tapping Mode Force Microscopy Experiments. *Nanotechnology* **2015**, *26*, 185706.
- (21) Maivald, P.; Butt, H. J.; Gould, S. A. C.; Prater, C. B.; Drake, B.; Gurley, J. A.; Elings, V. B.; Hansma, P. K. Using Force Modulation to Image Surface Elasticities with the Atomic Force Microscope. *Nanotechnology* **1991**, *2*, 103–106.
- (22) Rosa-Zeiser, A.; Weilandt, E.; Hild, S.; Marti, O. The Simultaneous Measurement of Elastic, Electrostatic and Adhesive Properties by Scanning Force Microscopy: Pulsed-Force Mode Operation. *Meas. Sci. Technol.* **1997**, *8*, 1333–1338.
- (23) Trtik, P.; Kaufmann, J.; Volz, U. On the Use of Peak-Force Tapping Atomic Force Microscopy for Quantification of the Local Elastic Modulus in Hardened Cement Paste. *Cem. Concr. Res.* **2012**, *42*, 215–221.
- (24) Dokukin, M. E.; Sokolov, I. Quantitative Mapping of the Elastic Modulus of Soft Materials with HarmoniX and PeakForce QNM AFM Modes. *Langmuir* **2012**, *28*, 16060–16071.
- (25) Wang, D.; Nakajima, K.; Fujinami, S.; Shibasaki, Y.; Wang, J. Q.; Nishi, T. Characterization of Morphology and Mechanical Properties of Block Copolymers Using Atomic Force Microscopy: Effects of Processing Conditions. *Polymer* **2012**, *53*, 1960–1965.
- (26) Lorenzoni, M.; Evangelio, L.; Verhaeghe, S.; Nicolet, C.; Navarro, C.; Pérez-Murano, F. Assessing the Local Nanomechanical Properties of Self-Assembled Block Co-Polymers Thin Films by Peak Force Tapping. *Langmuir* **2015**, *31*, 11630–11638.
- (27) Lorenzoni, M.; Evangelio, L.; Nicolet, C.; Navarro, C.; San Paulo, A.; Rius, G.; Pérez-Murano, F. Nanomechanical Properties of Solvent Cast Polystyrene and Poly(methyl Methacrylate) Polymer Blends and Self-Assembled Block Copolymers. *J. Micro/Nanolithogr., MEMS, MOEMS* **2015**, *14*, 033509–5.
- (28) Schön, P.; Bagdi, K.; Molnár, K.; Markus, P.; Pukánszky, B.; Julius Vancso, G. Quantitative Mapping of Elastic Moduli at the Nanoscale in Phase Separated Polyurethanes by AFM. *Eur. Polym. J.* **2011**, *47*, 692–698.
- (29) Nečas, D.; Klapetek, P. Gwyddion: An Open-Source Software for SPM Data Analysis. *Open Phys.* **2012**, *10*, 181–188.
- (30) Otsu, N. A Threshold Selection Method from Gray-Level Histograms. *IEEE Trans. Syst. Man. Cybern.* **1979**, *9*, 62–66.
- (31) Gharbi, A.; Tiron, R.; Argoud, M.; Chevalier, X.; Barros, P. P.; Nicolet, C.; Navarro, C. Contact Holes Patterning by Directed Self-Assembly of Block Copolymers: Process Window Study. *J. Micro/Nanolithogr., MEMS, MOEMS* **2015**, *14*, 023508.